3D-printed microneedle-based potentiometric sensor for pH monitoring in skin interstitial fluid

# 3D-printed microneedle-based potentiometric sensor for pH monitoring in skin interstitial fluid

Marc Parrilla,[a,b,*] Andres Vanhooydonck,[c] Maby Johns,[a,d] Regan Watts,[c] Karolien De Wael[a,b,*]

[a] A-Sense Lab, Department of Bioscience Engineering, University of Antwerp, Groenenborgerlaan 171, 2020 Antwerp, Belgium

[b] NANOlab Center of Excellence, University of Antwerp, Groenenborgerlaan 171, 2020, Antwerp, Belgium

[c] Product Development Research Group, Faculty of Design Sciences, University of Antwerp, Ambtmanstraat 1, 2000 Antwerp, Belgium

[d] IDLab, Faculty of Applied Engineering, University of Antwerp—imec, Sint-Pietersvliet 7, 2000 Antwerp, Belgium

ABSTRACT

Wearable electrochemical sensors are driven by the user-friendly capability of continuous monitoring of key biomarkers for diagnostic or therapeutic operations. Particularly, microneedle (MN)-based sensors can access the interstitial fluid (ISF) in the dermis layer of skin to carry out on-body transdermal detection of analytes. Interestingly, 3D-printing technology allows for rapid and versatile prototyping reaching micrometer resolution. Herein, for the first time, we explore 3D-printed hollow MN patches (1 mm height x 1 mm base with 0.3 mm hole) which are modified with conductive inks to develop a potentiometric sensor for pH monitoring. First, the piercing capability of 3D-printed MN patches is demonstrated by using the parafilm model and their insertion in porcine skin. Subsequently, the hollow MNs are filled with conductive inks to engineer a set of microelectrodes. Thereafter, the working and reference electrodes are properly modified with polyaniline and polyvinyl butyral, respectively, toward a highly stable potentiometric cell. A full *in vitro* characterization is performed within a broad range of pH (i.e. pH 4 to pH 9). Besides, the MN sensor is analytically assessed in phantom gel and pierced on porcine skin to evaluate the resilience of the MN sensor. Finally, the MN sensor is pierced on the forearm of a subject and tested for its on-body monitoring capability. Overall, 3D-printed MN-based potentiometric sensing brings a versatile and affordable technology to minimally-invasively monitor key physiological parameters in the body.

KEYWORDS. Microneedle-based potentiometric sensor, pH sensor, 3D-printing, hollow microneedle array, transdermal sensing, wearable electrochemical sensor

HIGHLIGHTS

- A 3D-printed hollow microneedle array has been developed.
- A hollow microneedle patch has been functionalized towards a miniaturized pH sensor.
- The full analytical characterization including *in vitro* (phantom gel) and *ex vivo* (porcine skin) tests has been provided.
- The pH monitoring of interstitial fluid has been demonstrated on a subject's forearm.

## 1. Introduction

Today, wearable gadgets allow for the digitalization of a broad range of parameters from the human body or the environment. Indeed, commercial wearable devices are mainly focused on the monitoring of physical parameters such as position, heart rate, and movement [1,2]. Still, the holy grail is the democratization of biochemical monitoring by providing biosensing capabilities to wearable platforms. Fortunately, research efforts are being performed to bring wearable biosensors for the detection and monitoring of key analytes in non-invasive matrices [3] such as sweat [4], interstitial fluid (ISF) [5], or tears [6]. These wearable devices along with the use of artificial intelligence (AI) will empower the next generation of personalized clinical decision support systems that will enhance patient treatment and potentially prevent and predict disease emergence in the human body [7]. The age of digital health intervention will facilitate physicians' decision-making processes or even provide closed-loop systems consisting of sensing and delivery for self-sufficient disease management [8].

Wearable electrochemical sensors are widely used in wearable biosensing as they are the ideal transducer from the biochemical domain to the digital domain which can subsequently be directly integrated into proper data treatment and AI capabilities [9]. Besides, electrochemical sensors are excellent candidates as they are low-cost and can be produced at a mass scale [10]. However, in contrast with optical sensors in which a colorimetric reaction enables the analytical readout, electrochemical sensors need a power source to launch the analysis. Particularly, electrochemical sensors that use voltammetry techniques such as chronoamperometry [11] or square-wave voltammetry [12] for the detection of biomolecules might consume a high amount of power during continuous monitoring which hinders the lifetime of the battery in a miniaturized wearable device. For this reason, potentiometry as a passive electrochemical technique can play a role in wearable biosensing due to its low-power consumption [13,14]. Ultimately, the rise of energy harvesting systems integrated with electrochemical sensors can facilitate the next generation of wearable self-powered electrochemical devices which can autonomously gather biochemical information from our bodies without the need for exchanging batteries [15].

Wearable microneedle(MN)-based electrochemical sensors are bringing a new paradigm in continuous transdermal biomonitoring of biomarkers [5]. The monitoring of key analytes in ISF provides several advantages in biosensing: (i) it avoids the use of painful methods for blood extraction; (ii) it provides equivalent values of the target analytes from blood; (iii) the ISF matrix is less complex in terms of composition than blood; and (iv) it offers high body availability [16,17]. Different configurations can be utilized to reach the ISF for proper analysis: (i) the MN array being the sensor [18]; the sensor or electrode is embedded inside a hollow microneedle (HMN) [19], or (iii) a HMN array is used for the extraction of ISF toward the electrochemical sensor for the analysis [20].

MN-based electrochemical sensors have been mainly designed for their use under voltammetric configuration for the detection of drugs [21], glucose, lactate and ethanol [18]. In contrast, MN potentiometric sensors have been scarcely developed, although showing advantages such as being area-independent and low-power consumption. Potentiometric sensors based on solid MNs have been engineered to monitor pH [22], β-lactam antibiotics using pH change as an indirect indicator of the target [23], and potassium [24]. Some authors reported the use of needle-based potentiometric sensors (i.e. a multiplexed array of electrodes embedded in the tip of a regular hypodermic needle) enabling the detection of sodium and potassium in ISF [25] or a pH sensor for real-time detection of pH in mice cerebrospinal fluid [26] or rat brain [27]. However, the needles used cannot be considered as a MN sensing patch due to the size and shape of the devices which usually employ a functionalized regular hypodermic needle. Therefore, this kind of arrangement cannot be considered a MN type sensor.

pH has been a highly relevant biomarker for monitoring health status as its alteration influences many biological processes [28]. For example, pH has shown relevance as a biomarker in extracellular fluid for the detection of breast cancer [29], in exhaled breath for chronic obstructive pulmonary disease [30], or in ISF for diabetes mellitus regulation [31]. Importantly, pH has also been reported as a biomarker for the control and monitoring of wound healing [32,33]. In this direction, innovative wound dressings with pH sensing capabilities allow for continuous monitoring of the wound status which enables optimal wound care and avoids chronic wounds in hospitalized patients [34]. Advanced wearable sensors have been designed as bandages and patches that incorporate flexible potentiometric sensors as a reliable and simple technique for pH monitoring [35]. Moreover, a MN-based platform has been also reported for the mapping of peripheral artery disease by coating polyaniline (PANI) on the metallic MN array as a selective layer for pH sensing [22]. In contrast, our work embeds the pH sensor inside 3D-printed MNs to protect the sensor from the mechanical force exerted during the insertion, avoiding any potential damage to the electrode. Importantly, MN-based

pH sensors can also offer advantages in wound monitoring due to the irregularity of wounds which MNs can overcome by monitoring the pH at a certain depth and not only in the outer layer of the wound as regular dressings.

Herein, we present for the first time a 3D-printed HMN array as a wearable platform to develop miniaturized potentiometric sensors for the continuous monitoring of pH in ISF (**Fig. 1**). A highly versatile 3D-printing technique based on low-force stereolithography is employed to fabricate HMN arrays with MNs of 1mm height x 1 mm base with 0.3mm hole (**Fig. 1A**). Subsequently, MN arrays are functionalized with conductive materials to confer the pH sensing capability. Importantly, the 3D-printed MN arrays can pierce the skin which is evaluated by means of the parafilm test and porcine skin. To convert the MN array into a potentiometric sensor, the holes on the MNs are first filled with conductive pastes, and thereafter, PANI is used as the pH-sensitive layer. The embodiment of the electrodes inside the HMN is paramount to avoid damaging the electrode during the insertion in the skin (**Fig. 1B**). A full analytical characterization of the MN pH sensor is performed making emphasis on the reversibility to probe the ability of the MN sensor to monitor fluctuations. Besides, the analytical performance is assessed: (i) *in vitro* using a phantom gel mimicking different pHs, (ii) *ex vivo* by piercing the MN sensor in porcine skin to demonstrate the mechanical robustness, and last but not least, (iii) on-body by piercing the MN sensor on the forearm of a subject to monitor the ISF pH in real-time. Overall, the use of wearable 3D-printed platforms along with potentiometric sensors will provide an advent in the manufacturing of versatile MN patches of different shapes that will encourage the innovative development of wearable devices to detect and monitor a wide range of biomarkers relevant to personalized medicine (**Fig. 1C**).

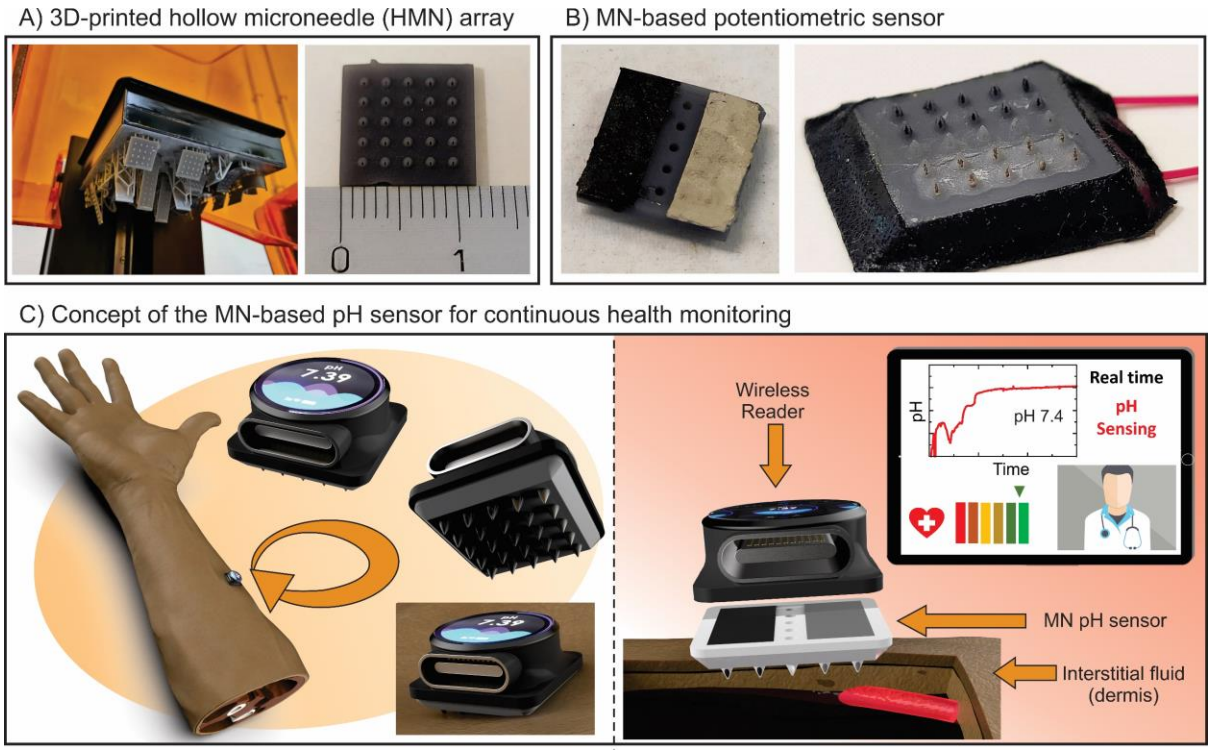


**Fig. 1.** Wearable 3D-printed microneedle-based potentiometric pH sensor. A) Fabrication of the 3D-printed hollow microneedle (HMN) array. B) Functionalization of the HMN array into a MN-based potentiometric sensor for pH monitoring showing the backside (left image) and frontside (right image) of the MN sensor. C) Concept of the MN-based pH sensor pierced on the forearm of a subject for the transdermal monitoring of pH and full connectivity to healthcare service.

## 2. Experimental section

### 2.1. Development of the MN potentiometric sensor

Hollow 3D-printed MN arrays (HMN) were designed as the platform to construct the potentiometric sensor (**Fig. 1**). Low-force stereolithography was utilized for the printing of the HMN as a 3D-printing technique that exhibits the highest resolution (25 µm) enabling the production of sharp HMNs (**Fig. 1A**). This form of rapid prototyping uses a focused laser to polymerize photo-curable resins. By moving up the z-axis, layers are cured and stacked to form objects with arbitrary geometry. This method provides excellent accuracy and reproducibility. Apart from the fabrication of MNs devices [36,37], 3D-printing has been used for the construction of electronics and electrochemical sensors [38,39], depicting the high versatility of this technique in several fields. **Fig. 2A and 2B** depict scanning electron microscopy images of the 3D-printed HMN array and a HMN, respectively. Interestingly, 3D printing offers high versatility allowing fast prototyping of different MN patches with conformable shapes (**Fig. S1**). Detailed information on

the evaluation of the piercing capability of the 3D-printed MN is described in the supplementary material. Besides, information on the fabrication and optimal parameters for the printing of the HMN array, as well as the materials and methods for their characterization are described in the supplementary material.

Once the HMN patch is printed, cured, and thoroughly rinsed with ethanol and water to remove any residues, half of the HMN array (10 MNs) was filled with a conductive paste (i.e. 50/50% graphite and paraffin oil) for the working electrode (**Fig. 1B** and **Fig. S2A**) and the other half of the HMN array (10 MNs) was filled with commercial Ag/AgCl paste (**Fig. 1B** and **Fig. S2B**). Once the hole of each MN is filled by using a spatula (**Fig. S2C**), the excess of the corresponding pastes was carefully removed from the hole using a scalpel following the angle of the MN (**Fig. S2D**). This is a critical step to avoid any paste above the MN as the polymeric material of the MN needs to protect the electrode. It is necessary to mention that the manufacturing of the MN sensor is currently performed manually. This is the reason for using a MN array that minimizes potential errors in a single MN electrode produced during manufacturing. Fortunately, the employment of a potentiometric sensing approach in which the analytical response does not depend on the area of the electrode minimizes the potential irreproducibility of the manual method. Still, the scalability of the production and functionalization of the MN array needs to be addressed in future work. Thereafter, Ag/AgCl paste was cured at 80 °C for 30 min in an oven. Electrical contacts were established using stainless steel wires connected at the backside of each of the conductive pastes to realize the working and reference electrode (**Fig. S2E**). Finally, the patch is placed on a PET substrate with the electrical contacts faced down and glued with silicon glue to cover the backside and secure robust electrical contacts that can withstand mechanical force during the piercing action (**Fig. 1B)**. Interestingly, the HMN array consisting of 25 HMNs can be also divided into multiple electrodes. In this work, we first divide the whole HMN array into two electrodes, and later into 8 electrodes. This latter configuration can provide future multiplexing capability to the MN sensor for the monitoring of multiple analytes by only the modification of each of the working electrodes.

To develop the MN potentiometric sensor for pH monitoring, the MN-based electrodes were functionalized by electrodeposition of PANI. Hence, cyclic voltammetry from -0.2 V to 1.2 V at a scan rate of 100 mV $s^{-1}$ (12 scans) in a solution of 0.1 M aniline and 1 M HCl was used for the electrodeposition of the PANI on the working electrode. The same procedure was repeated twice to generate a homogenous PANI layer. Subsequently, the MN sensor is rinsed with double-distilled water and stored overnight before use.

### 2.2. *In vitro* analytical characterization of the MN sensor

The analytical performance of the MN sensor was assessed by measuring the open circuit potential (OCP) between the reference electrode and the PANI-functionalized working electrode on the same MN platform. A set of Britton-Robinson buffer (BR) solutions from pH 4 to pH 10 was utilized to run all the experiments (e.g. calibration curve, repeatability, stability, reversibility). The electrochemical evaluation of the MN sensor was subsequently performed by drop-casting 100 µL of BR on the MN patch. A selectivity study was performed by adding the corresponding amount of the interferent (i.e. glycine, tyrosine, phenylalanine, paracetamol, caffeine, ascorbic acid, and uric acid) into the corresponding pH solution. The oxygen interference was performed by removing the dissolved oxygen from the solution using argon flow for 5 min in the solution. The temperature study was carried out by using a temperature-controlled bath. The biofouling study was accomplished by adding 20.6 g $L^{-1}$ of bovine serum albumin (BSA) as the average protein amount in ISF [40] on the BR solution.

A phantom gel mimicking skin test was carried out by using a hydrogel based on agarose (1.5 wt%) following a similar procedure found in the literature [21]. Briefly, the hydrogel was prepared by dissolving 150 mg of agarose in 10 mL of BR and stirring at 120 °C until a clear solution was obtained. Thereafter, the solution is poured into a glass Petri dish and allowed to solidify. After cooling down, the hydrogel is cut into pieces, immersed in different pH solutions, and let overnight to equilibrate. The potentiometric test was executed by piercing each hydrogel prepared with the suitable pH in the MN sensor.

### 2.3. *Ex vivo* analytical characterization of the MN sensor

Porcine skin was utilized to evaluate the mechanical resilience of the MN sensor and the robustness of the electrodes to withstand skin penetration. The *ex vivo* test consisted of inserting the MN sensor in the porcine skin by a simple application of thumb pressure with the MN tips piercing the skin (information about the skin preparation is described in the supplementary material), removing, and subsequently performing a calibration curve in solution. The comparison between a pre- and post-calibration curve exhibits the potential effects on the analytical performance of the MN sensor after the piercing action.

### 2.4. On-body test

The on-body test consists of applying the MN sensor on the forearm of a subject. This test is essential to show the feasibility of the MN sensor reaching the ISF and monitoring its pH. In this case, a 34-year-old male participant (i.e. weight of 73 kg and height of 1.89 m) was selected. First, the forearm area of the subject is rinsed with ethanol to remove remaining residues from sweat (e.g. fatty acids, electrolytes) that might be deposited on the skin and can interfere with the attachment of the MN patch, and dried with paper tissue. Subsequently, the MN patch is pushed towards the skin by the thumb to pierce the skin, and fixed with medical-grade tape

(Leukoplast, Essity, Sweden) to maintain the MN patch inserted in the skin. Proper adhesion of the patch with medical-grade tape is essential after piercing the skin to avoid detachment of the MN sensor. It is essential to mention that the MN patch has been thoroughly rinsed with buffer solution during the characterization steps and no chemical residue should remain on the polymeric MNs (e.g. uncured resin). After piercing and attaching the MN sensor, the device is ready to gather analytical data. The potentiometric readout is stabilized after ca. 2.5 min after the insertion and the predicted pH values from the ISF are calculated based on a previous off-body calibration curve that considers the temperature influence (i.e. calibration curve obtained at 32.5 °C). Finally, the MN sensor is removed after the test and the skin is monitored to evaluate potential effects on the skin.

## 3. Results and discussion

### 3.1. Design and piercing capability of the 3D-printed HMN array

Recently, huge interest has been raised in employing rapid prototyping techniques such as 3D printing to manufacture HMNs for biomedical applications [36]. In this direction, a comparison between different 3D-printing techniques based on digital light processing showed stereolithography as one of the methods for optimal HMNs with piercing capabilities [41]. However, most of the efforts have been focused on MNs for drug delivery [42]. In this article, 3D-printed HMNs are first characterized to enable a wearable platform suitable to pierce the skin and allow ISF sensing purposes (**Fig. 2A** and **2B**). The dimensions of the CAD model are 12 X 12 mm baseplate with 5 X 5 HMNs with a pitch of 2 mm between HMNs (**Fig. S3**). The size of each HMN is 1 X 1 mm (height x HMN base) and a tip of 100 µm with a hole of 300 µm diameter at one side of the MN (**Fig. S3**). **Fig. S4A** and **S4B** show optical images of the 3D-printed HMNs at front and side views, respectively. The sharpness of the 3D-printed MNs is compromised by the resolution of the 3D-printing technique, but having the advantage of being a rapid prototyping method. Although it exists some deviation from the CAD original model (i.e. height 10%, width 2%, tip 3.5%, and hole 1.8% N=3) (**Table S1**), the external dimensions of the HMNs show excellent performance of the 3D-printing method.

First, the mechanical robustness of the 3D-printed HMNs was evaluated in compression mode by applying 40 N for 30 s by using a texture analyzer constructed in-house (**Fig. S5A** and **S5B**) (detailed information in the supplementary material). The aforementioned parameters are an efficient method to evaluate MN failure as typical forces of less than 40 N are exerted during pressing with the thumb [43,44]. No apparent deformation was observed by optical microscopy on the MNs after the applied force (i.e. before mechanical test height of 1055.5 ± 21.0 µm and a tip of 92.1 ± 9.5 µm (N=4) and after mechanical test height of 1041.8 ± 13.2

μm and a tip of 78.4 ± 5.4 μm) (N=4). Besides, the parafilm holes after the test exhibited a diameter of 947.5 ± 35.9 μm (N=4) which is aligned with the diameter of the HMN at the base (ca. 1000 μm) (**Fig. S5C-S5F**). The insertion capability of the HMN array was subsequently evaluated by the well-established parafilm test [43] and the porcine skin test [20]. The parafilm test was executed by pressing the 3D-printed MNs patch onto the parafilm layers (8 X 127 μm) through a simple application of thumb pressure with the MN tips piercing through the film layers (**Fig. 2C**). Thereafter, the HMN patch is removed (**Fig. S6A**), and the holes in each layer are numbered and accounted for the penetration depth (**Fig. S6B**). **Fig. 2D** displays that 84.0 ± 10.6 % of the HMNs were able to penetrate up to 381 μm (three parafilm layers), meaning that the HMNs should be able to pierce the epidermis (ca. 120 μm thick) and reach the ISF in the dermis layer [45]. No apparent deformation of the HMNs was observed after the test (**Fig. S6C**). Similar insertion behavior was obtained with optimal 3D-printed MNs when applying a force of 32 N [41]. To evaluate the piercing capability in porcine skin (500 ± 100 μm of thickness), a similar procedure was applied with the application of thumb pressure with the MN tips piercing through the epidermis layer of the skin (N=3) (**Fig. S7A** and **S7B**). **Fig. 2E** and **Fig. S7C** depict the pierced skin patch after the removal of the HMN patch in three different patches. HMNs successfully penetrated the porcine skin (97.3 ± 4.6 %) and even penetrate the parafilm layer below (82.7 ± 6.1 %) (**Fig. 2F**). Therefore, the 3D-printed HMNs demonstrate the capability of piercing skin and their potential use as a wearable platform for electrochemical sensing.

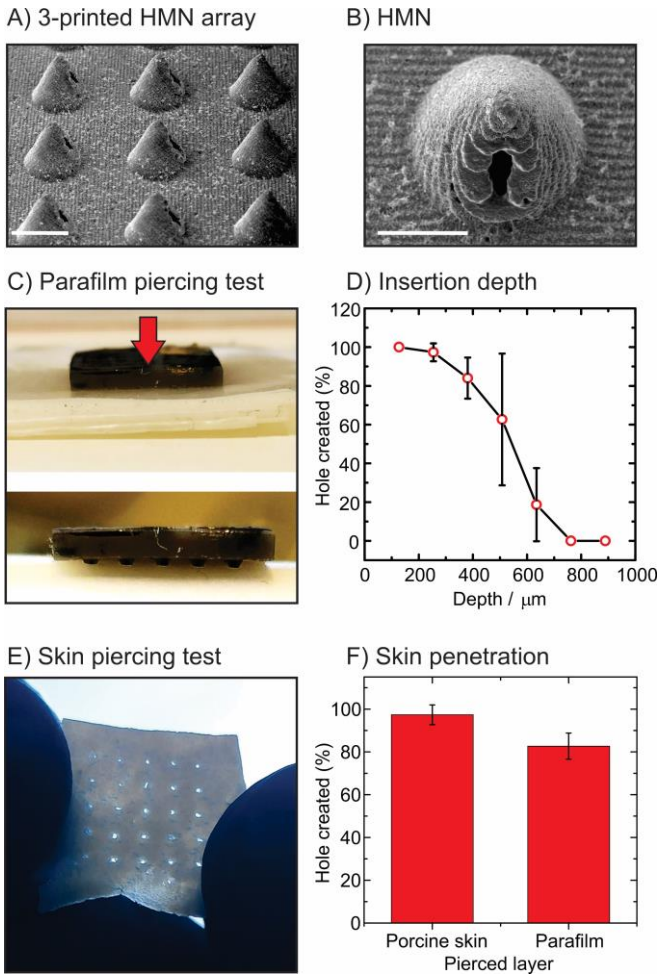


**Fig. 2.** Evaluation of the piercing capability of the 3D-printed MN array. A) SEM image of the HMN array. Scale 1 mm. B) SEM image of a HMN. Scale 500 µm. C) Parafilm test consisting of 8 stacked layers of the film and the application of the MN patch towards the film by applying force with the thumb finger. D) Penetration depth of the MN patch calculated from the holes created on the parafilm layers (1 parafilm layer = 127 µm). E) Image of porcine skin after the insertion with the MN patch. F) Penetration of the MN array on the skin and the parafilm layer below the skin.

### 3.2. Analytical characterization of the MN potentiometric sensor

Here, we report for the first time the development of a 3D-printed HMN-based potentiometric sensor. The beauty of potentiometry is that it employs a two-electrode system that can monitor the difference in OCP raised between the working (which change the OCP according to the analyte of interest) and the reference electrode (which keeps a constant voltage) [13]. Hence, the modification of the holes of the 3D-printed HMN patch with conductive materials is essential to first produce a working (WE) and (pseudo)reference electrode (RE). Hence, graphite-based paste and Ag/AgCl paste were used to fill half of the MN holes to obtain a HMN patch in which half of the patch worked as a RE and the other half as a WE (**Fig. S2**). **Fig.**

**S4C** and **Fig. S4E** display the images of the WE and RE, respectively. To confer selectivity to the WE toward pH monitoring, the electrodeposition of PANI was executed by cyclic voltammetry with 0.1 M aniline solution in acidic media (1M HCl) [46]. PANI is a conductive polymer whose ability to monitor protons is based on the transition between emeraldine salt to emeraldine base [47]. **Fig. S8A-C** displays the electrodeposition setup and the corresponding cyclic voltammograms. **Fig. S4D** shows an optical image of a homogenous layer of electrodeposited PANI on the functionalized WE. SEM characterization was also performed to deeply visualize the PANI nanotube formation on the WE (**Fig. S9A-C**). Moreover, the RE was also modified with a polyvinyl butyral (PVB) layer to enhance its stability and avoid voltage fluctuations from changes in the biofluid composition (**Fig. S4F**). A layer is created on top of the RE (**Fig. S10**) which maintains a constant concentration of chloride ions at the interface of the Ag/AgCl electrode while performing as a bridge between the electrolyte inside the membrane and the sample [24].

First, the analytical performance of each electrode was separately evaluated. The MN working electrode and MN reference electrode were interrogated against a glass reference electrode upon changes in the pH of the solution. **Fig. S11A** exhibits the time traces of three consecutive calibration curves on the WE from pH 10 to pH 4, with its corresponding average calibration curve (**Fig. S11B**) presenting a near-Nernstian behavior (i.e. 56.1 ± 0.5 mV $pH^{-1}$) within a linear range from pH 9 to pH 5. Moreover, the stability of the WE was evaluated at pH 6 showing 1.4 mV $h^{-1}$ drift over 9 h (**Fig. S11C**). The performance of the RE was evaluated in **Fig. S12A** by changing the pH of the solutions. In this case, two conditions were assessed: (i) only with the Ag/AgCl paste; and (ii) with PVB coated RE. **Fig. S12B** shows improved performance of the PVB coated RE (i.e. slope of -0.45 mV $pH^{-1}$ against -0.68 mV $pH^{-1}$). Besides, the PVB-coated RE exhibited a drift of 1.1 mV $h^{-1}$ (**Fig. S12C**). Hence, PVB-coated RE was used for its integration with the WE toward a complete electrochemical cell.

Once the MN potentiometric sensor is built (**Fig. 3A**), the potentiometric response of the MN sensor was assessed by changing the pH of the buffer solutions on the MN patch. The time of response of the MN sensor was 50 s to reach 90% of the change in OCP (**Fig. 3B**). The analytical response was evaluated by changing the buffer solution from pH 10 to pH 4. **Fig. 3C** shows the overlapped time traces from three consecutive calibration curves with the corresponding calibration curve in **Fig. 3D** (N=3). The MN pH sensor exhibited a linear relationship ($y=-0.059x+0.419$, $R^2=0.99$) between pH 9 to pH 5 which fits within the indicator range for wound healing [32,33]. The ability to detect fluctuations in pH is essential for continuous monitoring of the wound status or other medical conditions. For this reason, a reversibility test was performed from pH 9 to pH 5 for 5 cycles (**Fig. 3E**). An outstanding performance was obtained showing a highly reproducible slope of -67.2 ± 1.0 mV $pH^{-1}$ and an

intercept of 489.2 ± 10.1 mV (N=10) (**Fig. 3F**). Operational stability is a key issue when using a wearable device for continuous monitoring. In this sense, long-term monitoring was evaluated at pH 4.7 and pH 5.9 showing a drift of -0.75 mV $h^{-1}$ during 9 h and 0.59 mV $h^{-1}$ during 17 h, respectively. Although the stability test was performed using a 200 µL drop in an enclosed environment, the evaporation led to an OCP change in the pH of the drop which can be seen when the OCP was back into the initial values after adding fresh solution (**Fig. S13**).

The selectivity of the MN pH sensor was assessed by adding regular biomolecules encountered in biofluids (200 µM glycine, 200 µM tyrosine, 200 µM phenylalanine, 50 µM ascorbic acid, and 200 µM uric acid) as well as exogenous molecules that can be ingested during daily activities (i.e. 50 µM paracetamol, 50 µM caffeine) during a potentiometric measurement in pH 6 (**Fig. 3G**). Constant OCP values were observed after the addition of each interference, thus demonstrating the suitability of the PANI-based layer to monitor pH in biofluids.

Temperature is a factor to consider when designing skin patches as it can influence the electrochemical response as determined by the Nernst equation [13]. Hence, the pH response was evaluated at 21.5 °C and 32.5 °C which is the average temperature of the skin [48]. **Fig. 3H** and **3I** show the time trace and calibration curve at these temperatures. The linear relationships deviate according to the temperature displaying a slope $T_{21.5°C}$ of -61.0 mV $pH^{-1}$ with an intercept of 467.2 mV and a slope $T_{32.5°C}$ of -66.2 mV $pH^{-1}$ with an intercept of 487.9 mV. Albeit the differences are narrow, it is essential to consider this factor when dealing with an on-body test, as typically the calibration curve of the sensor is performed out of the body at room temperature and the on-body test is executed at skin temperature (**Fig. 3J**). Therefore, a correction factor needs to be applied to increase the accuracy of the monitoring system. The analytical performance of the MN sensor in anaerobic and aerobic conditions was also evaluated. Therefore, the potentiometric response was recorded under environmental conditions and by pumping argon into the solution for 5 min to remove oxygen (**Fig. 3K**). See in the plot small shifts at each pH solution because the OCP recording was stopped during the time in which oxygen is removed. When comparing the calibration curves (**Fig. 3L**), almost all data points overlapped showing no influence from the oxygen (i.e. aerobic conditions displayed a slope of -67.6 mV $pH^{-1}$ and an intercept of 504 mV and anaerobic conditions a slope of -67.5 mV $pH^{-1}$ and an intercept of 510 mV).

Polyaniline as an organic conducting polymer has proven to overcome biofouling issues [49]. Hence, the biofouling on the MN sensor was assessed by performing a reversibility test from pH 8 to pH 5 (**Fig. 3M**) with and without 20.6 g $L^{-1}$ of BSA in pH solutions. This amount of albumin is selected as the total protein in ISF [40]. **Fig. 3N** displays the corresponding calibration curves with and without albumin in solution showing only a deviation of 2.3% on

the slope and of 3.0% on the intercept, meaning a negligible effect of the protein adsorption on the PANI electrode. It is worth mentioning that PANI has demonstrated biocompatibility, and more importantly, PANI does not induce any sensitization and skin irritation which makes it an excellent candidate for wearable devices [50], explaining why PANI has been successfully used in many biomedical applications [51]. Besides, several sterilization processes have been shown to keep the properties of PANI [52], which is essential for the use of the MN pH sensor as a potential medical device. Last but not least, integration with a portable and wireless OCP reader is necessary for the full wearability of the device. **Fig. S14A** depicts an image of a portable reader connected to the MN pH sensor. The OCP output of the portable reader was compared with a benchtop potentiostat upon changes in pH (**Fig. S14B**). Both devices exhibited similar OCP values leading to a linear range between pH 8 to pH 4 with only a deviation of 6.7% on the slope and of 4.1% on the intercept (**Fig. S14C**). Thus, the wireless reader shows promises to be used for wearable purposes.

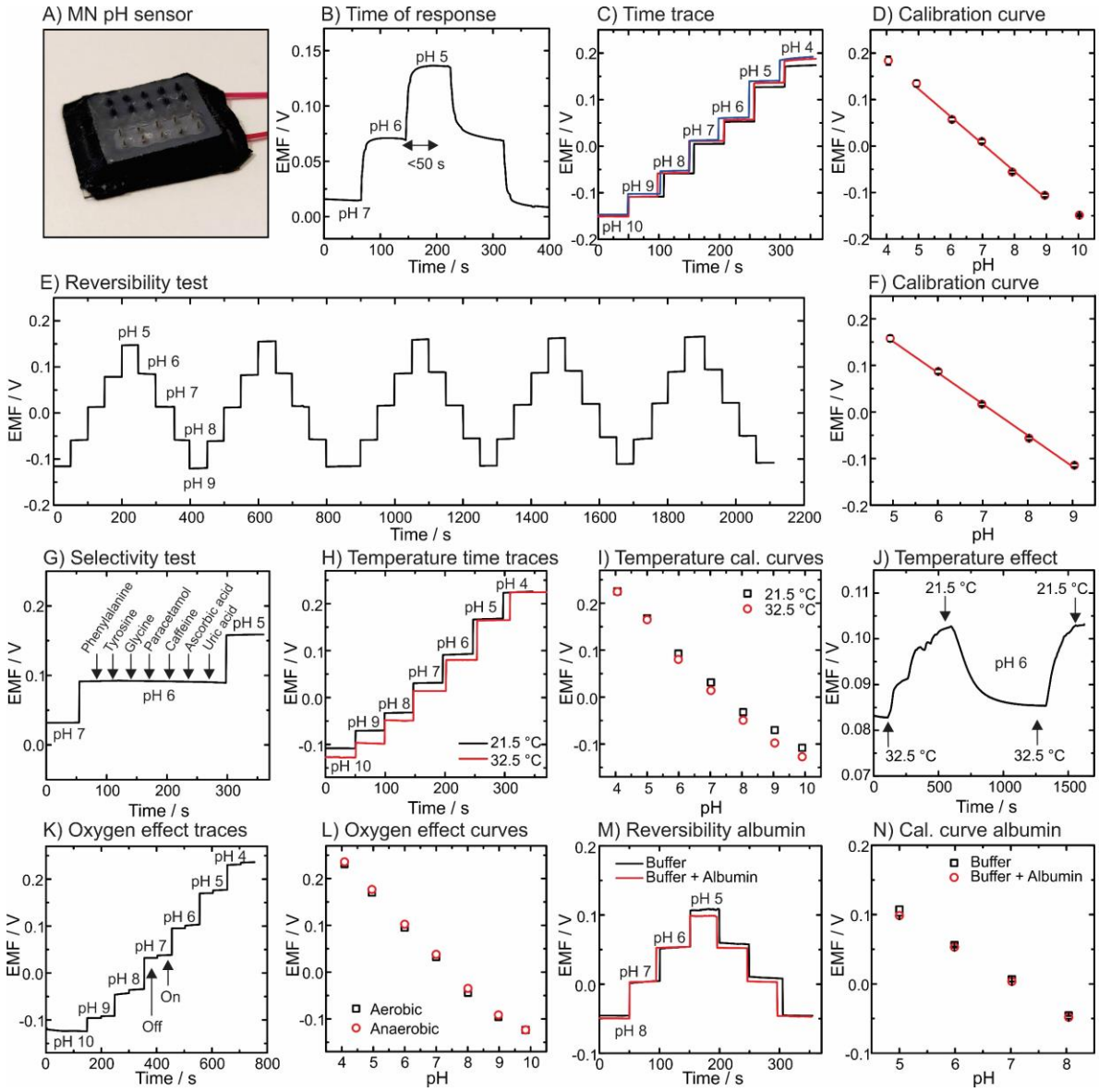

**Fig. 3.** Analytical performance of the MN-based potentiometric pH sensor. A) Image of the MN pH sensor. B) Time of response upon a change in the pH of the solution. B) Potentiometric traces upon increasing pH of three consecutive assays using the same MN pH sensor, and C) corresponding calibration curves from pH 10 to pH 4 (N=3). E) Reversibility test upon increasing and decreasing pH solutions from pH 9 to pH 5 during 5 cycles, and F) corresponding calibration curves (N=10). G) Selectivity test consisting of adding each of the interferents into a pH 6 solution: 200 µM glycine, 200 µM tyrosine, 200 µM phenylalanine, 50 µM paracetamol, 50 µM caffeine, 50 µM ascorbic acid, and 200 µM uric acid. H) Temperature effect on the potentiometric response, I) corresponding calibration curves at 21.5 °C and 32.5 °C, and J) temperature effect upon increasing and decreasing temperatures from room temperature to skin temperature in pH 6. K) Effect of the oxygen present in the potentiometric response, and L) corresponding calibration curve with and without oxygen. The removal of the oxygen was executed by pumping argon into the solution. M) Evaluation of the biofouling on the MN pH sensor by adding albumin (20.6 g $L^{-1}$) in the pH solution, and N) corresponding calibration curve obtained from the reversibility test with high protein content in the pH solution.

### 3.3. *In vitro* characterization in skin-mimicking phantom gel

The use of skin-mimicking phantom gel is a widely used test to characterize the ability of the MN sensors to pierce and maintain the analytical properties [21]. Hence, a hydrogel with agarose at 1.5% in BR solution was prepared and let to equilibrate in each pH solution to build a set of hydrogels from pH 10 to pH 4. During the test, the MN pH sensor was pierced on the hydrogel at the suitable pH (**Fig. 4A**), and subsequently, the OCP was recorded for ca. 50 s (**Fig. 4B**). The calibration curves were performed first in buffer solution followed by two consecutive curves using the hydrogel approach to assess the analytical performance in the phantom gel. **Fig. 4C** displays similar potentiometric responses obtained in the solution and the phantom gel. The corresponding calibration curves exhibited a slope of 67.7 ± 2.3 mV $pH^{-1}$ with an intercept of 574.5 ± 21.1 mV within linearity between pH 8 to pH 4 (**Fig. 4D**). The reversibility test using phantom gel was also evaluated. **Fig. 4E** shows the results between increasing and decreasing pH values (i.e. pH 8 to pH 5) obtained by changing the phantom gels. The corresponding calibration curve is represented in the calibration plot (i.e. slope of 66.7 ± 4.1 mV $pH^{-1}$ with an intercept of 595.4 ± 17.1 mV) (**Fig. 4F**) that depicts the reversibility of the pH monitoring. It is worth mentioning that an increment in the deviation of the potential was observed in basic pH (i.e. pH 8). It is suggested that the agarose gel might influence the limit of detection of the MN sensor and hinder the monitoring of low proton concentration in comparison to the reversibility test in **Fig. 3E** in which excellent repeatability at basic pHs was obtained. Another reason might be that the MN sensor response is hindered when the MN electrode is pierced. For this reason, the next step is to evaluate the influence of the piercing

action on the porcine skin (i.e. *ex vivo* test). Overall, the MN pH sensor demonstrates favorable behavior when dealing with skin-mimicking gels, and thus, promising results for on-body monitoring.

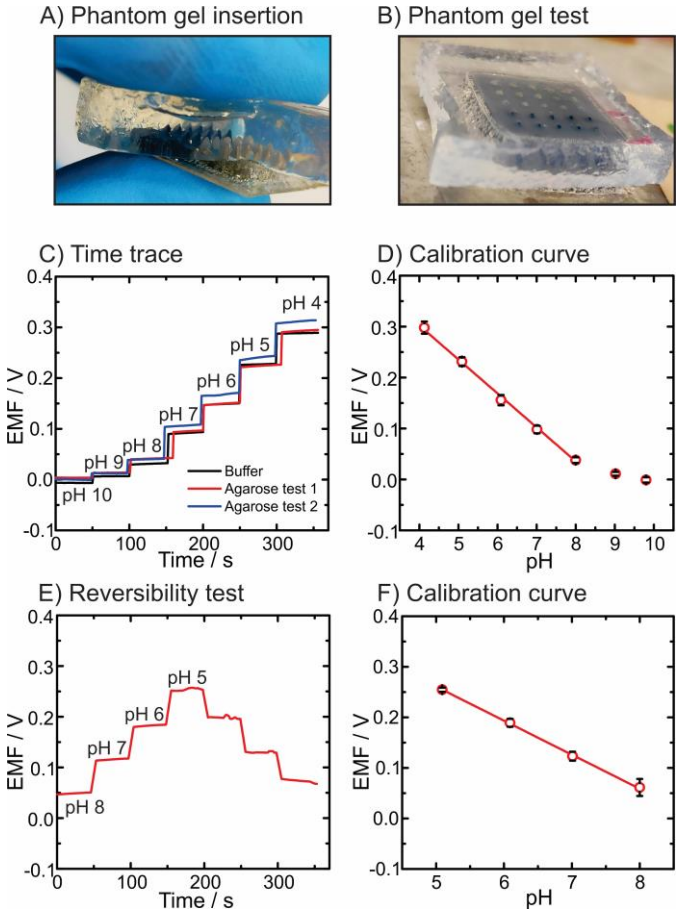


**Fig. 4.** In vitro analytical characterization of the MN-based potentiometric pH sensor in the phantom gel. A) Image of the phantom gel based on agarose pierced on the MN pH sensor. B) Setup of the solid-state potentiometric measurement by using phantom gels at different pHs. C) Potentiometric response of the MN pH sensor in buffer and inserted in the phantom gel (twice), and D) corresponding calibration curve. E) Potentiometric response of the reversibility test by exchanging hydrogels with different pHs, and F) corresponding calibration curve.

Another valuable feature of MN sensors is the ability to multiplex. In this way, a patch with multiple MNs can be functionalized separately to realize several sensors in the same MN patch. In this setup, the 3D-printed MN patch that worked as a potentiometric sensor was divided into four electrochemical cells with only two MNs as WE and two MNs as RE in each cell (**Fig. S15A**). The preparation of the MN sensors consisted of filling the HMNs in four columns instead of using two columns as depicted in **Fig. S2** and dividing accordingly to create

four independent pH sensors after the individual electrodeposition of PANI. **Fig. S15B** displays a reversibility test from pH 8 to pH 4, and the corresponding calibration curve in **Fig. S15C** exhibits a slope of -63.7 ± 0.8 mV $pH^{-1}$ and an intercept of 499 ± 7.2 mV (N=8). Therefore, the calibration curves exhibited high reproducibility among the pH sensors obtained immediately after the functionalization.

### 3.4. Evaluation of MN potentiometric sensor robustness with *ex vivo* test

To proceed further in the evaluation of the potential of the 3D-printed MN pH sensor to be utilized in a real scenario, the mechanical resiliency of the MN pH sensor was assessed by an *ex vivo* test (**Fig. 5A**). The test consisted of interrogating the MN pH sensor in pH solutions before and after applying the piercing action to porcine skin (**Fig. 5B**). The *ex vivo* test was carried out on two different MN pH sensors. **Fig. 5C** and **5E** display the potentiometric responses before and after the piercing action exhibiting similar analytical performance. Accordingly, **Fig. 5D** and **5F** depict the calibration plots showing differences in the OCP at each pH solution before and after insertion in porcine skin between 14.6 to 1.9 % from pH 8 to pH 4 for the MN pH sensor 1, and between 6.6 to 0.7 % from pH 8 to pH 4 for the MN pH sensor 2. These narrow deviations prove the resiliency of the MN sensor setup to mechanical insertion. MN pH sensor 1 showed a linear relationship from pH 4 to pH 8 and MN pH sensor 2 from pH 4 to pH 7. It is worth mentioning that MN patch 2 previously showed a decrease in the performance at alkaline pH before and after the insertion, thus exhibiting no loss of performance due to the piercing activity. The robustness of the MN pH sensor relies on the embodiment of the pH electrode on the hole of the MN, meaning that the body of the MN performs the piercing action avoiding the surface of the PANI layer to be damaged. Moreover, the use of potentiometric sensors is highly advantageous in miniaturized sensing platforms such as MNs patches as the electrochemical response does not depend on the electrode's area in contact with the solution. Hence, the analytical readout from the MN sensor can be even recorded when only one MN from the array reaches the solution. In a real scenario, the MN sensing patch is pierced in the skin, but even if some MNs from the array would not have successfully reached the ISF, the potentiometric readout would indicate the pH value of the ISF. In contrast, MN sensors based on voltammetric techniques, which readout is area-dependent, need to assure a full insertion in the skin for accurate monitoring.

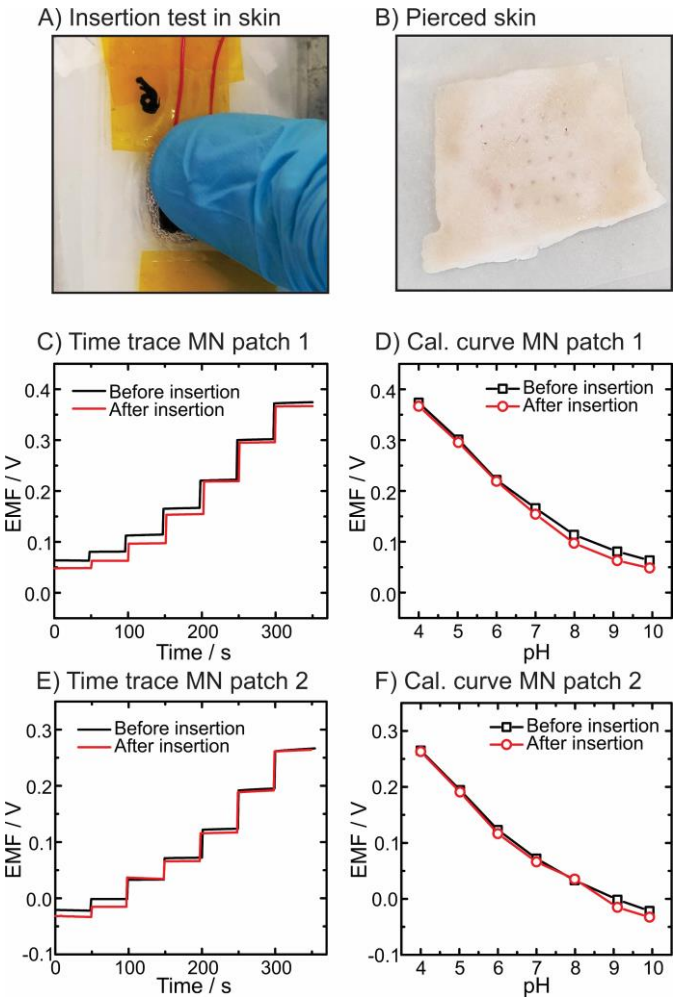


**Fig. 5.** Ex vivo analytical characterization of the MN-based potentiometric pH sensor in porcine skin. A) Image of the ex vivo test by pushing the MN pH sensor toward the skin. B) Image of the porcine skin after piercing with the MN pH sensor. C) and E) Potentiometric responses of the MN pH sensor before and after the insertion in the porcine skin using two different MN pH sensors, and D) and F) comparison of calibration curves before and after the ex vivo test of the two MN pH sensors.

### 3.5. Assessment of the ability to continuously monitor pH in ISF: on-body test

To validate the potential of the MN pH sensor to be used as a wearable device for transdermal pH monitoring, an on-body test was carried out by placing the MN pH sensor on the forearm of a volunteer (**Fig. 6A**). The on-body performance of the MN pH sensor was assessed by piercing the MN patch on the forearm and monitoring the OCP while the patch was inserted into the skin (**Fig. 6B**). The expected pH value obtained should be ca. pH 7.4 as the pH of the ISF is the same as for physiological pH [40]. A preliminary calibration from pH 8 to pH 6 was executed off-body. After 100 s from the insertion, the OCP readout was stabilized indicating that the ISF reached the MN pH sensor. According to the calibration, the OCP from the on-

body test reveals a pH value of pH 7.56 ± 0.02 calculated from 300 to 500 s OCP in the plot. However, this prediction was performed by considering the off-body calibration curve executed at room temperature (i.e. 21.5 °C). To be more accurate in the pH monitoring, a temperature factor needs to be applied as the wearable MN patch is now placed in contact with the skin at ca. 32.5 °C. From our preliminary temperature characterization (**Fig. 3H** and **3I**), temperature factors from the slope and intercept were calculated. Subsequently, these factors were applied to the off-body calibration curve and a new prediction was attained. Hence, a pH value of pH 7.39 ± 0.01 from 300 to 500 s presented a closer value to the expected pH value of 7.4 in the ISF of a healthy subject. The errors from the expected potential value (in pH 7.4) were 7.04 % and 0.32 % without and with applying the temperature factor, respectively. Therefore, temperature correction is essential to improve the accuracy of pH monitoring in a future scenario. The future integration of a miniaturized temperature sensor is needed to assure suitable pH monitoring, particularly during an outdoor activity where the temperature of skin might be altered. Last but not least, time-lapse images of the human subject's forearm were taken after the removal of the MN patch (**Fig. 6D**). The images indicated that after 10 min almost no evidence of the MN pH sensor, thus demonstrating no skin irritation or inflammation in the applied area. The use of the biocompatible PANI along with commercially approved polymers widely used in biomedical devices, position 3D-printed MN sensors as promising tools for diagnostics and monitoring. Long-term tests and skin observation are depicted as prospects to further evaluate the suitability of the MN potentiometric sensors as wearable devices for continuous on-body monitoring of health status.

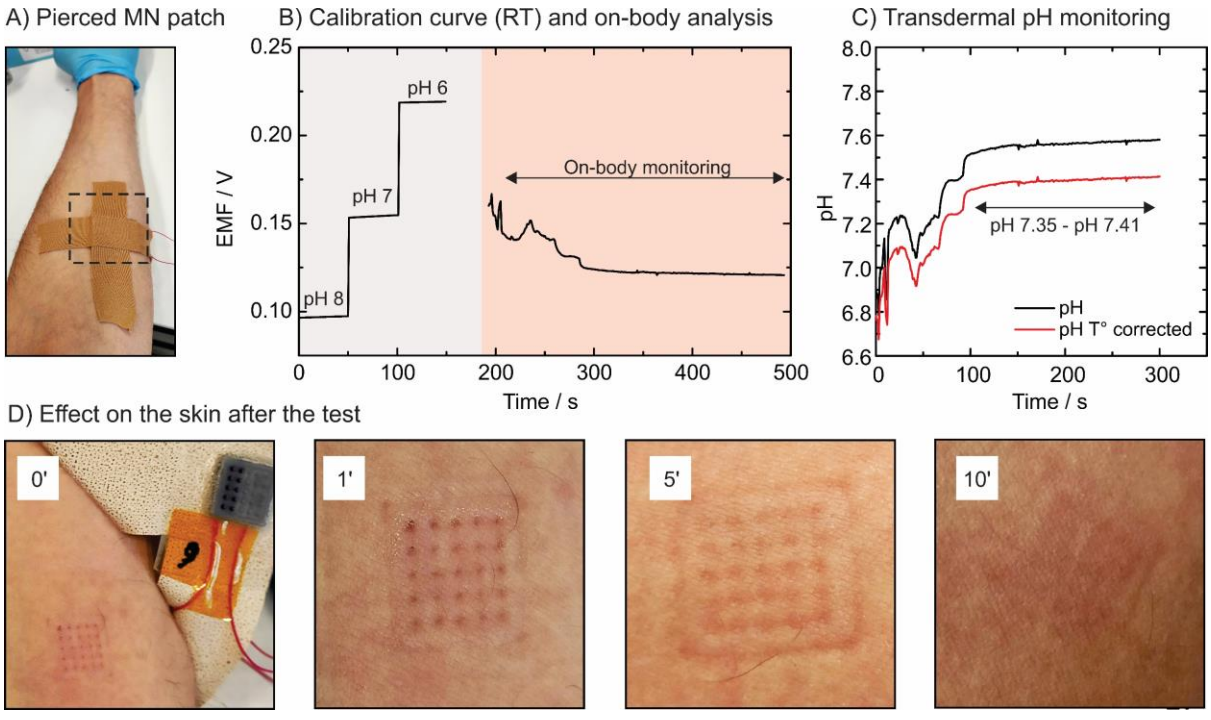

**Fig. 6.** On-body test. A) Image of the MN pH sensor pierced on the forearm of a subject. B) Potentiometric response of a preliminary calibration curve out of the body and subsequent on-body analysis while the MN pH sensor is inserted in the forearm. C) Prediction of the interstitial fluid pH (transdermal pH monitoring) with and without temperature correction. D) Effect of the piercing of the MN pH sensor on the skin after removal of the MN patch at different times. RT=room temperature.

## 4. Conclusions

We have demonstrated, for the first time, the development of MN-based potentiometric sensors based on 3D-printed hollow microneedles. The 3D-printed HMNs were first evaluated for piercing capability. Thereafter, a novel strategy for the modification of the HMNs to realize a potentiometric cell with the prospect of multiplexing has been described. Importantly, a full analytical characterization in solution, *in vitro* employing skin-mimicking phantom gel, *ex vivo* using porcine skin, and finally, on-body by piercing in a human subject's forearm proves the outstanding performance of the MN pH sensor. The temperature needs to be considered when using the MN devices in on-body tests as it plays an essential role in the OCP output. The MN pH sensor exhibited a Nernstian response within a wide linear range (i.e. pH 8 to pH 4) suitable for monitoring the pH of ISF as well as the pH during wound healing. The latter case offers advantages in terms of a wide clinical range minimizing the error from the potentiometric sensor in a highly relevant clinical issue. The potentiometric design can offer great advantages in MN sensors: (i) the response is independent of the area of the electrode, thus offering feasible miniaturization; connected to this property, (ii) a MN potentiometric array offers multiplexing capability while exhibiting the same analytical performance, and last but not least (iii) potentiometry is a low-power consumption technique which enables continuous monitoring at the same time that enlarges the lifetime of the device. Overall, future efforts will be devoted to the miniaturization of the 3D-printed MNs to facilitate the insertion behavior, the extension of the potentiometric approach to other analytes, and enlarging and assessing the long-term monitoring of analytes to enable a wearable device that will promote a radical shift from episodic to continuous healthcare.

## Credit author statement

**Marc Parrilla:** Conceptualization, methodology, investigation, data curation, writing -original draft, writing - review & editing. **Andres Vanhooydonck**: Conceptualization, methodology.

**Maby Johns:** methodology. **Regan Watts**: resources. **Karolien De Wael:** Investigation, resources, project administration, writing - review and editing.

## Declaration of competing interest

The authors declare that they have no known competing financial interests or personal relationships that could have appeared to influence the work reported in this paper.

## Acknowledgments

The authors acknowledge financial support from the University of Antwerp, Bijzonder Onderzoeksfonds (41-FA070500-FFB210098) and Bijzonder Onderzoeksfonds (DOCPRO) (41 - FA118000 - FFB200007 and FFB210300), Belgium, and the Fund for Scientific Research (FWO) Flanders, Medium-scale Research Infrastructure (MZW 2018, Screen printing facilities and high-resolution Raman imaging of (printed) surfaces and materials), Belgium.

Appendix A. Supplementary data

Supplementary data to this article can be found online at xxx.

## References

[1] Kenry, J.C. Yeo, C.T. Lim, Emerging flexible and wearable physical sensing platforms for healthcare and biomedical applications, Microsystems Nanoeng. 2 (2016) 16043. https://doi.org/10.1038/micronano.2016.43.

[2] J. Choi, R. Ghaffari, P. Gutruf, A.J. Bandodkar, S. Krishnan, J.A. Rogers, L. Tian, T.R. Ray, Bio-Integrated Wearable Systems: A Comprehensive Review, Chem. Rev. 119 (2019) 5461–5533. https://doi.org/10.1021/acs.chemrev.8b00573.

[3] N. Promphet, S. Ummartyotin, W. Ngeontae, P. Puthongkham, N. Rodthongkum, Non-invasive wearable chemical sensors in real-life applications, Anal. Chim. Acta. 1179 (2021) 338643. https://doi.org/10.1016/j.aca.2021.338643.

[4] P. Yang, G. Wei, A. Liu, F. Huo, Z. Zhang, A review of sampling, energy supply and intelligent monitoring for long-term sweat sensors, Npj Flex. Electron. 6 (2022) 1–13. https://doi.org/10.1038/s41528-022-00165-9.

[5] H. Teymourian, F. Tehrani, K. Mahato, J. Wang, Lab under the Skin: Microneedle Based Wearable Devices, Adv. Healthc. Mater. 10 (2021) 2002255. https://doi.org/10.1002/adhm.202002255.

[6] X. Ma, S. Ahadian, S. Liu, J. Zhang, S. Liu, T. Cao, W. Lin, D. Wu, N.R. de Barros,

M.R. Zare, S.E. Diltemiz, V. Jucaud, Y. Zhu, S. Zhang, E. Banton, Y. Gu, K. Nan, S. Xu, M.R. Dokmeci, A. Khademhosseini, Smart Contact Lenses for Biosensing Applications, Adv. Intell. Syst. 3 (2021) 2000263. https://doi.org/10.1002/aisy.202000263.

[7] H. Haick, N. Tang, Artificial Intelligence in Medical Sensors for Clinical Decisions, ACS Nano. 15 (2021) 3557–3567. https://doi.org/10.1021/acsnano.1c00085.

[8] J. Li, J.Y. Liang, S.J. Laken, R. Langer, G. Traverso, Clinical Opportunities for Continuous Biosensing and Closed-Loop Therapies, Trends Chem. 2 (2020) 319–340. https://doi.org/10.1016/j.trechm.2020.02.009.

[9] Y. Lin, M. Bariya, A. Javey, Wearable Biosensors for Body Computing, Adv. Funct. Mater. 31 (2021) 2008087. https://doi.org/10.1002/adfm.202008087.

[10] K. Mahato, J. Wang, Electrochemical Sensors: From the Bench to the Skin, Sensors Actuators B Chem. 344 (2021) 130178. https://doi.org/10.1016/j.snb.2021.130178.

[11] I. Algov, A. Feiertag, R. Shikler, L. Alfonta, Sensitive enzymatic determination of neurotransmitters in artificial sweat, Biosens. Bioelectron. 210 (2022) 114264. https://doi.org/10.1016/j.bios.2022.114264.

[12] M. Parrilla, A. Vanhooydonck, R. Watts, K. De Wael, Wearable wristband-based electrochemical sensor for the detection of phenylalanine in biofluids, Biosens. Bioelectron. 197 (2022) 113764. https://doi.org/10.1016/j.bios.2021.113764.

[13] M. Parrilla, M. Cuartero, G.A. Crespo, Wearable potentiometric ion sensors, TrAC - Trends Anal. Chem. 110 (2019) 303–320. https://doi.org/10.1016/j.trac.2018.11.024.

[14] J. Bobacka, A. Ivaska, A. Lewenstam, Potentiometric ion sensors, Chem. Rev. 108 (2008) 329–351. https://doi.org/10.1021/cr068100w.

[15] M. Parrilla, K. De Wael, Wearable Self-Powered Electrochemical Devices for Continuous Health Management, Adv. Funct. Mater. 31 (2021) 2107042. https://doi.org/10.1002/adfm.202107042.

[16] J. Heikenfeld, A. Jajack, B. Feldman, S.W. Granger, S. Gaitonde, G. Begtrup, B.A. Katchman, Accessing analytes in biofluids for peripheral biochemical monitoring, Nat. Biotechnol. 37 (2019) 407–419. https://doi.org/10.1038/s41587-019-0040-3.

[17] P.P. Samant, M.M. Niedzwiecki, N. Raviele, V. Tran, J. Mena-Lapaix, D.I. Walker, E.I. Felner, D.P. Jones, G.W. Miller, M.R. Prausnitz, Sampling interstitial fluid from human skin using a microneedle patch, Sci. Transl. Med. 12 (2020) eaaw0285.

https://doi.org/10.1126/SCITRANSLMED.AAW0285.

[18] F. Tehrani, H. Teymourian, B. Wuerstle, J. Kavner, R. Patel, A. Furmidge, R. Aghavali, H. Hosseini-Toudeshki, C. Brown, F. Zhang, K. Mahato, Z. Li, A. Barfidokht, L. Yin, P. Warren, N. Huang, Z. Patel, P.P. Mercier, J. Wang, An integrated wearable microneedle array for the continuous monitoring of multiple biomarkers in interstitial fluid, Nat. Biomed. Eng. (2022). https://doi.org/10.1038/s41551-022-00887-1.

[19] A.M.V. Mohan, J.R. Windmiller, R.K. Mishra, J. Wang, Continuous minimally-invasive alcohol monitoring using microneedle sensor arrays, Biosens. Bioelectron. 91 (2017) 574–579. https://doi.org/10.1016/j.bios.2017.01.016.

[20] M. Parrilla, U. Detamornrat, J. Domínguez-Robles, R.F. Donnelly, K. De Wael, Wearable Hollow Microneedle Sensing Patches for the Transdermal Electrochemical Monitoring of Glucose, Talanta. 249 (2022) 123695. https://doi.org/10.1016/j.talanta.2022.123695.

[21] K.Y. Goud, K. Mahato, H. Teymourian, K. Longardner, I. Litvan, J. Wang, Wearable Electrochemical Microneedle Sensing Platform for Real-Time Continuous Interstitial Fluid Monitoring of Apomorphine: Toward Parkinson Management, Sensors Actuators B Chem. 354 (2022) 131234. https://doi.org/10.1016/j.snb.2021.131234.

[22] W. Lee, S.H. Jeong, Y.W. Lim, H. Lee, J. Kang, H. Lee, I. Lee, H.S. Han, S. Kobayashi, M. Tanaka, B.S. Bae, Conformable microneedle pH sensors via the integration of two different siloxane polymers for mapping peripheral artery disease, Sci. Adv. 7 (2021) eabi6290. https://doi.org/10.1126/sciadv.abi6290.

[23] S.A.N. Gowers, D.M.E. Freeman, T.M. Rawson, M.L. Rogers, R.C. Wilson, A.H. Holmes, A.E. Cass, D. O'Hare, Development of a Minimally Invasive Microneedle-Based Sensor for Continuous Monitoring of β-Lactam Antibiotic Concentrations in Vivo, ACS Sensors. 4 (2019) 1072–1080. https://doi.org/10.1021/acssensors.9b00288.

[24] M. Parrilla, M. Cuartero, S. Padrell, M. Rajabi, N. Roxhed, F. Niklaus, G.A. Crespo, Wearable All-Solid-State Potentiometric Microneedle Patch for Intradermal Potassium Detection, Anal. Chem. 91 (2019) 1578−1586. https://doi.org/10.1021/acs.analchem.8b04877.

[25] H. Li, G. Wu, Z. Weng, H. Sun, R. Nistala, Y. Zhang, Microneedle-Based Potentiometric Sensing System for Continuous Monitoring of Multiple Electrolytes in Skin Interstitial Fluids, ACS Sensors. 6 (2021) 2181–2190.

https://doi.org/10.1021/acssensors.0c02330.

[26] G.K. Mani, K. Miyakoda, A. Saito, Y. Yasoda, K. Kajiwara, M. Kimura, K. Tsuchiya, Microneedle pH Sensor: Direct, Label-Free, Real-Time Detection of Cerebrospinal Fluid and Bladder pH, ACS Appl. Mater. Interfaces. 9 (2017) 21651–21659. https://doi.org/10.1021/acsami.7b04225.

[27] J.-X. Zhou, F. Ding, L.-N. Tang, T. Li, Y.-H. Li, Y.-J. Zhang, H.-Y. Gong, Y.-T. Li, G.-J. Zhang, Monitoring of pH Change in Live Rat Brain with MoS2/PAN Functionalized Microneedle, Analyst. 143 (2018) 4469–4475. https://doi.org/10.1039/C8AN01149D.

[28] E. Proksch, pH in nature, humans and skin, J. Dermatol. 45 (2018) 1044–1052. https://doi.org/10.1111/1346-8138.14489.

[29] M. Chen, C. Chen, Z. Shen, X. Zhang, Y. Chen, F. Lin, X. Ma, C. Zhuang, Y. Mao, H. Gan, P. Chen, X. Zong, R. Wu, Extracellular pH is a biomarker enabling detection of breast cancer and liver cancer using CEST MRI, Oncotarget. 8 (2017) 45759–45767. https://doi.org/10.18632/oncotarget.17404.

[30] W. MacNee, S.I. Rennard, J.F. Hunt, L.D. Edwards, B.E. Miller, N.W. Locantore, R. Tal-Singer, Evaluation of exhaled breath condensate pH as a biomarker for COPD, Respir. Med. 105 (2011) 1037–1045. https://doi.org/10.1016/j.rmed.2011.02.009.

[31] Y. Marunaka, Roles of interstitial fluid pH in diabetes mellitus: Glycolysis and mitochondrial function, World J. Diabetes. 6 (2015) 125. https://doi.org/10.4239/wjd.v6.i1.125.

[32] L. Alexander, S. Andreas, S. Grabbe, J. Dissemond, Influence of pH on wound-healing: a new perspective for wound-therapy?, Arch. Dermatological Res. 298 (2007) 413–420. https://doi.org/10.1007/s00403-006-0713-x.

[33] G. Power, Z. Moore, T. O'Connor, Measurement of pH, exudate composition and temperature in wound healing: A systematic review, J. Wound Care. 26 (2017) 381–397. https://doi.org/10.12968/jowc.2017.26.7.381.

[34] Q. Zeng, X. Qi, G. Shi, M. Zhang, H. Haick, Wound Dressing : From Nanomaterials to Diagnostic Dressings and Healing Evaluations, ACS Nano. 16 (2022) 1708–1733. https://doi.org/10.1021/acsnano.1c08411.

[35] M.S. Brown, B. Ashley, A. Koh, Wearable technology for chronic wound monitoring: Current dressings, advancements, and future prospects, Front. Bioeng. Biotechnol. 6 (2018) 47. https://doi.org/10.3389/fbioe.2018.00047.

[36] U. Detamornrat, E. McAlister, A.R.J. Hutton, E. Larrañeta, R.F. Donnelly, The Role of 3D Printing Technology in Microengineering of Microneedles, Small. (2022) 2106392. https://doi.org/10.1002/smll.202106392.

[37] N.U. Rajesh, I. Coates, M.M. Driskill, M.T. Dulay, K. Hsiao, D. Ilyin, G.B. Jacobson, J.W. Kwak, M. Lawrence, J. Perry, C.O. Shea, S. Tian, J.M. DeSimone, 3D-Printed Microarray Patches for Transdermal Applications, JACS Au. (2022) 10.1021/jacsau.2c00432. https://doi.org/10.1021/jacsau.2c00432.

[38] B.C. Gross, J.L. Erkal, S.Y. Lockwood, C. Chen, D.M. Spence, Evaluation of 3D Printing and Its Potential Impact on Biotechnology and the Chemical Sciences., Anal. Chem. (2014). https://doi.org/10.1021/ac403397r.

[39] H. Ota, S. Emaminejad, Y. Gao, A. Zhao, E. Wu, S. Challa, K. Chen, H.M. Fahad, A.K. Jha, D. Kiriya, W. Gao, H. Shiraki, K. Morioka, A.R. Ferguson, K.E. Healy, R.W. Davis, A. Javey, Application of 3D Printing for Smart Objects with Embedded Electronic Sensors and Systems, Adv. Mater. Technol. 1 (2016) 1600013. https://doi.org/10.1002/admt.201600013.

[40] N. Fogh-Andersen, B.M. Altura, B.T. Altura, O. Siggaard-Andersen, Composition of interstitial fluid, Clin. Chem. 41 (1995) 1522–1525.

[41] E. Mathew, G. Pitzanti, A.L. Gomes Dos Santos, D.A. Lamprou, Optimization of printing parameters for digital light processing 3d printing of hollow microneedle arrays, Pharmaceutics. 13 (2021) 1–14. https://doi.org/10.3390/pharmaceutics13111837.

[42] N. Elahpour, F. Pahlevanzadeh, M. Kharaziha, H.R. Bakhsheshi-Rad, S. Ramakrishna, F. Berto, 3D printed microneedles for transdermal drug delivery: A brief review of two decades, Int. J. Pharm. 597 (2021) 120301. https://doi.org/10.1016/j.ijpharm.2021.120301.

[43] E. Larrañeta, J. Moore, E.M. Vicente-Pérez, P. González-Vázquez, R. Lutton, A.D. Woolfson, R.F. Donnelly, A proposed model membrane and test method for microneedle insertion studies, Int. J. Pharm. 472 (2014) 65–73. https://doi.org/10.1016/j.ijpharm.2014.05.042.

[44] I.A. Tekko, G. Chen, J. Domínguez-Robles, R. Raj Singh Thakur, I.M.N. Hamdan, L. Vora, E. Larrañeta, J.C. McElnay, H.O. McCarthy, M. Rooney, R.F. Donnelly, Development and characterisation of novel poly (vinyl alcohol)/poly (vinyl pyrrolidone)-based hydrogel-forming microneedle arrays for enhanced and sustained transdermal

delivery of methotrexate, Int. J. Pharm. 586 (2020) 119580. https://doi.org/10.1016/j.ijpharm.2020.119580.

[45] S.L. Avon, R.E. Wood, Porcine skin as an in-vivo model for ageing of human bite marks, J. Forensic Odontostomatol. 23 (2005) 30–39.

[46] A.J. Bandodkar, V.W.S. Hung, W. Jia, G. Valdés-Ramírez, J.R. Windmiller, A.G. Martinez, J. Ramírez, G. Chan, K. Kerman, J. Wang, Tattoo-based potentiometric ion-selective sensors for epidermal pH monitoring., Analyst. 138 (2013) 123–8. https://doi.org/10.1039/c2an36422k.

[47] T. Lindfors, A. Ivaska, Raman based pH measurements with polyaniline, J. Electroanal. Chem. 580 (2005) 320–329. https://doi.org/10.1016/j.jelechem.2005.03.042.

[48] W. Bierman, The temperature of the skin surface, JAMA - J. Am. Med. Assoc. 106 (1936) 1158–1162. https://doi.org/10.1001/jama.1936.02770140020007.

[49] M.J. Russo, M. Han, P.E. Desroches, C.S. Manasa, J. Dennaoui, A.F. Quigley, R.M.I. Kapsa, S.E. Moulton, R.M. Guijt, G.W. Greene, S.M. Silva, Antifouling Strategies for Electrochemical Biosensing: Mechanisms and Performance toward Point of Care Based Diagnostic Applications, ACS Sensors. 6 (2021) 1482–1507. https://doi.org/10.1021/acssensors.1c00390.

[50] P. Humpolicek, V. Kasparkova, P. Saha, J. Stejskal, Biocompatibility of polyaniline, Synth. Met. 162 (2012) 722–727. https://doi.org/10.1016/j.synthmet.2012.02.024.

[51] E.N. Zare, P. Makvandi, B. Ashtari, F. Rossi, A. Motahari, G. Perale, Progress in Conductive Polyaniline-Based Nanocomposites for Biomedical Applications: A Review, J. Med. Chem. 63 (2020) 1–22. https://doi.org/10.1021/acs.jmedchem.9b00803.

[52] J. Stejskal, M. Trchov, J. Ku, Z. Cap, P. Humpolí, J. Proke, Effect of sterilization techniques on the conductivity of polyaniline and polypyrrole, Synth. Met. 282 (2021) 116937. https://doi.org/10.1016/j.synthmet.2021.116937.